Energy Storage Materials 39 (2021) 239–249

Contents lists available at ScienceDirect

Energy Storage Materials

journal homepage: www.elsevier.com/locate/ensm

Conversion-alloying dual mechanism anode: Nitrogen-doped carbon-coated Bi_2Se_3 wrapped with graphene for superior potassium-ion storage

Kuan-Ting Chen [b], Shaokun Chong [a,*], Lingling Yuan [a], Yi-Chun Yang [b], Hsing-Yu Tuan [b,*]

[a] Frontiers Science Center for Flexible Electronics, Xi'an Institute of Flexible Electronics and Xi'an Institute of Biomedical Materials & Engineering, Northwestern Polytechnical University, Xi'an 710072, PR China

[b] Department of Chemical Engineering, National Tsing Hua University, Hsinchu 30013, Taiwan

ARTICLE INFO

Keywords:
Potassium-ion battery
Anode material
Conversion-alloying mechanism
Bismuth selenide

ABSTRACT

The construction of an anode material with a conversion-alloying dual mechanism will facilitate the development of potassium-ion batteries (PIBs) with high-energy density. Here a Bi_2Se_3 nanosheets coated with nitrogen-doped carbon and wrapped with reduced graphene oxide (Bi_2Se_3@NC@rGO) is fabricated to boost K-ion storage. The Bi_2Se_3@NC@rGO composite with strong C–O–Bi bonding can provide superior electrode integrity and electrochemical kinetics by combining the synergistic effect of carbon encapsulation and graphene confinement. *In situ* X-ray diffraction and *ex situ* transmission electron microscopy analyses demonstrate that K-ion intercalation/deintercalation proceeds *via* both conversion and alloying/dealloying reactions based on 12-electron transfer per formula unit; the conversion product of K_2Se can efficiently suppress the volume expansion during alloying/dealloying process to improve its stability. Hence, a high reversible capacity of 612.0 mAh·g^{-1} at 100 mA·g^{-1}; a great rate capability with the capacity of 101.6 mAh·g^{-1} at 5 A·g^{-1}, and an ultra-long cycling life of over 1000 cycles at 500 mA·g^{-1} is achieved for the Bi_2Se_3@NC@rGO. The K-ion full cell is also assembled using $K_2Ni[Fe(CN)_6]$ as the cathode, thereby contributing a high-energy density of 162.9 Wh·kg^{-1} at 10 mA·g^{-1} and a great cyclability.

1. Introduction

Lithium-ion batteries have been considered one of the most competitive electric energy storage (EES) devices due to their high-energy density, high power density, and good cycling stability [1,2]. However, the problem of lithium resource shortage is escalating, thereby necessitating the development of an alternative rechargeable EES technology using the abundant resources of the earth's crust. Sodium and potassium, as adjacent family elements of lithium, have attracted extensive attention due to their rich reserves and low cost [3–5]. Compared to Na^+/Na (−2.71 V *vs.* standard hydrogen electrode), the redox potential of K^+/K (−2.93 V) is much closer to Li^+/Li (−3.04 V), and a much lower value for K^+/K can be obtained in a propylene-carbonate electrolyte solvent compared to Li^+/Li [6–10]. Given this, potassium-ion batteries (PIBs) can contribute to higher operating voltage and energy density than sodium-ion batteries. Besides, PIBs can deliver superior electrochemical kinetics and higher rate capability due to weaker Lewis acidity of K-ion than Li- and Na-ion in a nonaqueous electrolyte [11,12]. Therefore, investigating the suitability of some electrode materials to accommodate large-sized K-ions (1.38 Å) will promote the development of PIBs as large-scale stationary EES equipment [13,14].

In recent years, research on cathode materials for PIBs has emerged in an endless stream. Among them, layered oxides, polyanion compounds, organics, and Prussian blue analogs showed good K-ion storage performances, and their electrochemical reaction mechanism has been deeply studied [15–17]. For the anode materials, three types of electrodes were generally studied, and their reactions with potassium ions including the intercalation process, conversion reaction, and alloying mechanism [14,18,19]. The intercalated anode materials (such as graphite, amorphous carbon, etc.) usually have excellent cycling performance; nevertheless, slow diffusion kinetics and the use of a binary intercalation compound with less potassium have caused poor rate capability and limited the specific capacity below 300 mAh·g^{-1} [20–22]. In contrast, higher specific capacities can be achieved for conversion reaction materials. However, high operating voltage will significantly reduce the energy density of K-ion full cell, as well as poor rate property and cycling stability are also obtained due to the low electrical conductivity and large volume expansion [23–25]. The anode materials (*e.g.*, Sb, Bi, Sn, P, Pb, and Ge) based on alloying mechanism present ultra-high specific capacity and low-working voltage [26–28], thereby contributing high-energy density; whereas, a huge volume change will cause the electrode to break up and gradually lose its activity upon cy-

* Corresponding authors.
E-mail addresses: iamskchong@nwpu.edu.cn (S. Chong), hytuan@che.nthu.edu.tw (H.-Y. Tuan).

https://doi.org/10.1016/j.ensm.2021.04.019
Received 13 January 2021; Received in revised form 31 March 2021; Accepted 11 April 2021
Available online 20 April 2021

cling. Meanwhile, the inherent electron and ion transport ability also needs to be further improved to obtain higher power density.

To study the anode materials with outstanding electrochemical performance and promising commercialization, the electrode with conversion-alloying dual mechanism has been considered to be promising [29–32]. This type of anode has a dual capacity contribution of cationic metal conversion reaction and elemental metal-alloying process, thereby presenting a higher specific capacity than a pure alloying mechanism material. Also, the participation of the alloying reaction ensures that the electrode material has a low average working voltage. Moreover, the conversion reaction product can act as a buffer zone to accommodate the volume expansion generated by the alloying process and effectively release the stress of the active material, thus maintaining the integrity of the electrode material. Therefore, exploring anode materials using a conversion-alloying dual mechanism is an effective way to further optimize the electrochemical properties, and this has great theoretical significance for understanding the K-ion storage mechanism.

Here, we proposed a novel Bi_2Se_3-based three-dimensional (3D) composite anode for PIBs with conversion-alloying dual mechanism, prepared *via* solvothermal, *in situ* polymerization, solution-phase, and sintering processes as illustrated in Fig. 1a, in which dopamine acted as N-doped C resource to encapsulate Bi_2Se_3 and graphene oxide was used for confinement. During these processes, the Bi_2Se_3 nanosheets were uniformly coated with N-doped carbon and confined by reduced graphene oxide (Bi_2Se_3@NC@rGO). The carbon-coating layer and graphene do not only act as a buffer area to restrain the strain from the large volume variation but also boost fast K-ion and electron transfer, thereby presenting excellent structural stability and good kinetic behavior. The results of *in situ* X-ray diffraction (XRD) and *ex situ* transmission electron microscopy (TEM) analyses confirmed that Bi_2Se_3@NC@rGO undergoes dual mechanism of conversion-alloying, thereby allowing 12 mol K-ion diffusion. Finally, a 3.0 V K-ion full battery displaying a high-energy density of 162.9 $Wh{\cdot}kg^{-1}$ at 10 $mA{\cdot}g^{-1}$ was fabricated with $K_2Ni[Fe(CN)_6]$ cathode and Bi_2Se_3@NC@rGO anode.

2. Experimental section

2.1. Materials

Bismuth (III) nitrate pentahydrate ($Bi(NO_3)_3{\cdot}5H_2O$, 99.999%), selenium (Se, 99.99%), polyvinylpyrrolidone (PVP) (Mw~55,000), dopamine hydrochloride, tri (hydroxymethyl) aminomethane (99.8%), oleic acid (OA, 90%), potassium metal (98%), 1-methyl-2-pyrrolidinone (NMP, anhydrous, 99.5%), diethyl carbonate (DEC, anhydrous, 99%), ethylene carbonate (EC, anhydrous, 99%), and potassium hexafluorophosphate (KPF_6, 99%) were purchased from Sigma-Aldrich. Nitric acid (69%–70%) was purchased from J.T. Baker; ethylene glycol (EG, 99%) was purchased from ACROS; graphene oxide (GO, 98%) was purchased from Golden Innovation Business Co., Ltd, and a glass fiber was purchased from Advantec. Poly(vinylene fluoride), Super P, and a coin-type cell CR2032 were purchased from Shining Energy.

2.2. Material Synthesis

2.2.1. Synthesis of Bi_2Se_3 nanosheets

Bi_2Se_3 nanosheets were synthesized *via* a facile hydrothermal method. 6 mmol of Se powder dissolved into 10 mL nitric acid. Then 2 mmol of $Bi(NO_3)_3{\cdot}5H_2O$ and 0.6 g PVP were dissolved into a mixed solution of 25 mL EG and 35 mL OA under stirring. Both of the above solutions were mixed and stirred for 20 min. The obtained suspension was transferred into a Teflon-lined stainless steel autoclave and kept at 180 °C for 24 h. After naturally cooling down to room temperature, the obtained precipitate was washed with ethanol and deionized water several times and collected by centrifugation before drying by rotary evaporation. The prepared pure Bi_2Se_3 was used as a precursor for coated composites.

2.2.2. Synthesis of Bi_2Se_3@NC nanosheet composites

To prepare the Bi_2Se_3@NC composite, 100 mg Bi_2Se_3 was dispersed in 150 mL 0.01 M Tris-buffer solution (pH=8.5) under sonication. Then, 50-mg dopamine hydrochloride powder was added and continuously stirred for 16 h. The polydopamine-coated Bi_2Se_3 was obtained by centrifugation, washed with deionized water and ethanol, subjected to a tube furnace, and then annealed at 500 °C for 3 h with a ramp rate of 5 °C/min under Argon flow to obtain Bi_2Se_3@NC composites.

2.2.3. Synthesis of Bi_2Se_3@rGO nanosheet composites

To prepare the Bi_2Se_3@rGO nanosheet composite, 60-mg Bi_2Se_3 and 20-mg GO nanosheets were dispersed in 20 and 10 mL of deionized water by sonication, respectively. Then, the mixture of the two resulting solutions was sonicated for another 2 h and frozen at −50 °C for 36 h. The Bi_2Se_3@rGO was prepared by annealing at 500 °C for 3 h with a ramp rate of 5 °C/min under Argon flow.

2.2.4. Synthesis of Bi_2Se_3@NC@rGO nanosheet composites

Polydopamine-coated Bi_2Se_3 was used as a precursor, and the same procedure for synthesizing Bi_2Se_3@rGO was repeated to obtain Bi_2Se_3@NC@rGO.

2.3. Material characterizations

The morphologies of as-synthesized materials were conducted using FESEM (HITACHI-SU8010) with EDS (HORIBA, EX-250), TEM (JEOL, ARM200F). XRD patterns were determined by a D8 ADVANCE X-ray diffractometer (Bruker) with Cu Kα radiation. Raman spectroscopy (Tokyo Instruments, Nanofinder 30) with a radiation of 633 nm. TGA analysis was obtained using a thermogravimetric analyzer (TA, Q50) from 50 to 700 °C with a heating rate of 10 °C/min in air. The BET surface area and pore distribution plots were measured by a Micromeritics ASAP 2020. The valence states of the samples were tested by high-resolution X-ray photoelectron spectra (ULVAC-PH PHI QuanteraII). AFM study was performed by BRUKER Dimension Icon.

2.3.1. Electrochemical Measurements

For the preparation of working electrodes, Bi_2Se_3, Bi_2Se_3@NC, Bi_2Se_3@rGO, and Bi_2Se_3@NC@rGO were mixed with Super P and PVDF binder in a weight ratio of 7:2:1 and dispersed in NMP to form a uniform slurry to further cast on the Cu foil. The average mass loading of the active material is ~1.0 $mg{\cdot}cm^{-2}$. The electrochemical properties of the as-prepared electrodes were evaluated by assembling CR 2032-type coin cells in the argon-filled glovebox. For the half-cell measurement, the investigated sample, potassium metal foil, and glass fiber were employed as the working electrode, counter electrode, and separator, respectively. For the full cell measurement, $K_2Ni[Fe(CN)_6]$ and Bi_2Se_3@NC@rGO were used as cathode and anode, respectively, and the anode was predischarged to eliminate the large initial irreversible capacity and supplement enough K resource. $K_2Ni[Fe(CN)_6]$ was prepared by a previously reported method [33]. The electrolyte was prepared by dissolving 0.8 M KPF_6 in EC/DEC (1:1, v/v). Galvanostatic charge/discharge tests were conducted on Maccor Series 4000 battery test system. CV and EIS tests were performed on a Biologic VMP3 electrochemistry workstation. The operando XRD patterns of Bi_2Se_3@NC@rGO were collected on a Bruker D8 ADVANCE diffractometer (Cu Kα) for three cycles. A current density of 50 $mA{\cdot}g^{-1}$ is selected for charging and discharging processes between 0.01–3.0 V (*vs.* K^+/K).

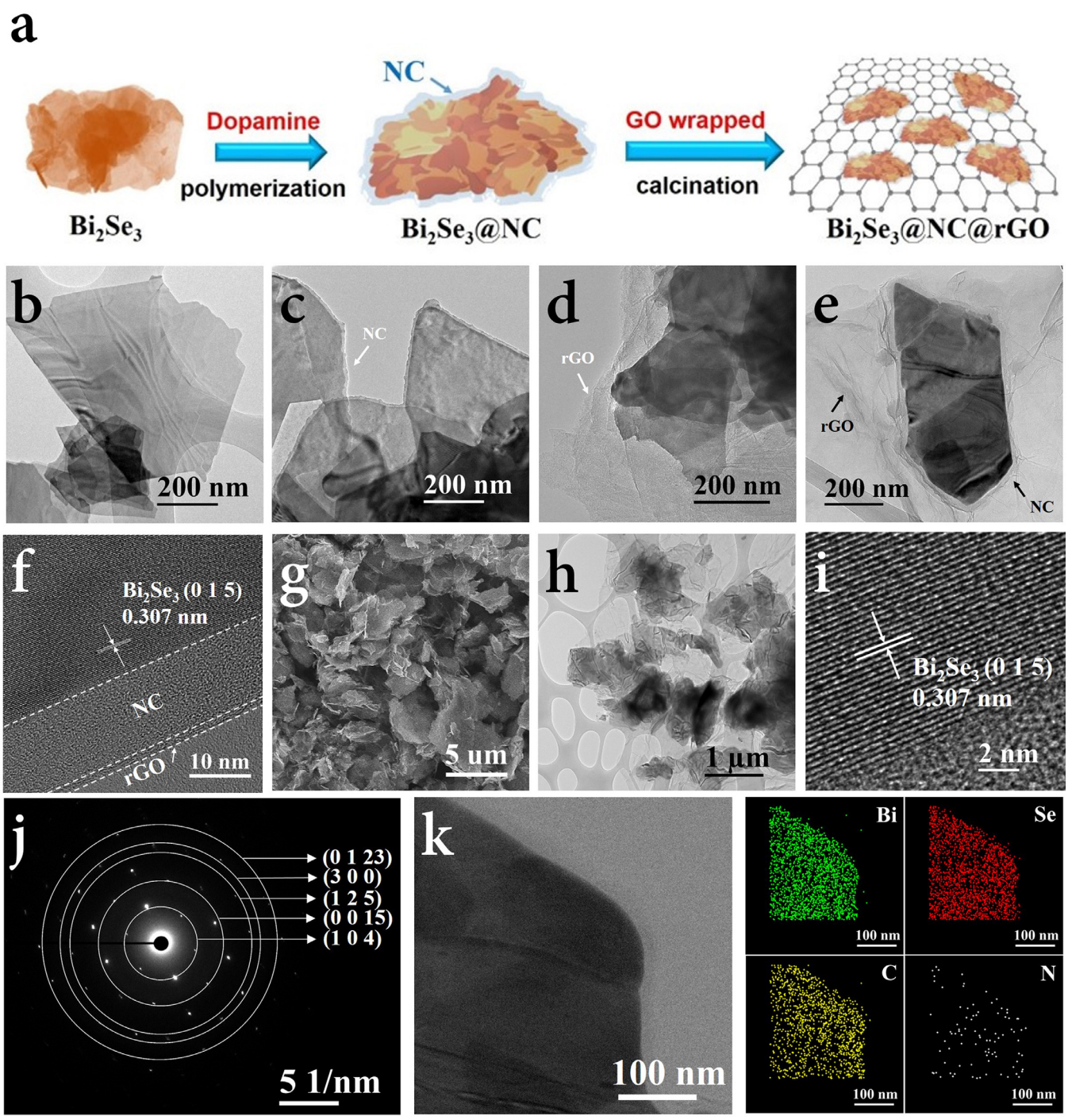

Fig. 1. Morphology and structure characterization: a) Schematic illustration drawing of the preparation process of triple-layer Bi_2Se_3@NC@rGO composite; TEM images of b) Bi_2Se_3, c) Bi_2Se_3@NC, d) Bi_2Se_3@rGO and e) Bi_2Se_3@NC@rGO; f) HRTEM image, g) FESEM image, h) TEM image, i) HRTEM image, j) SAED pattern and k) EDS elemental mapping images of Bi_2Se_3@NC@rGO.

3. Results and discussion

3.1. Morphology and structure characterization

The TEM image of pristine Bi_2Se_3, which was synthesized *via* a facile one-step solvothermal method, displays a thin nanosheet morphology as presented in Fig. 1b and Fig. S1a–d . The high-resolution TEM (HRTEM) image and selected area electron diffraction (SAED) pattern in Fig. S1e, h illustrate the single-crystalline nature of Bi_2Se_3. The atomic force microscopy (AFM) was employed to measure the thickness of Bi_2Se_3, whose result (Fig. S1f-g) shows that the thickness of Bi_2Se_3 is about 8 nm. The carbon coating was processed through *in situ* polymerization and sintering process to fabricate the nitrogen (N)-doped carbon-coated Bi_2Se_3 nanosheets (Bi_2Se_3@NC). As presented in Fig. 1c and Fig. S2a–c , a uniform carbon-coating layer with a thickness of above 10 nm grows on the surface of the Bi_2Se_3 nanosheets. A solution-phase assembly strategy, followed by a calcination procedure, was employed to wrap Bi_2Se_3 using reduced graphene oxide (Bi_2Se_3@rGO). An ultra-thin graphene-layer-confined Bi_2Se_3 nanosheet was presented in Fig. 1d and Fig. S3a–c . Therefore, the Bi_2Se_3@NC@rGO composite was fabricated *via* the

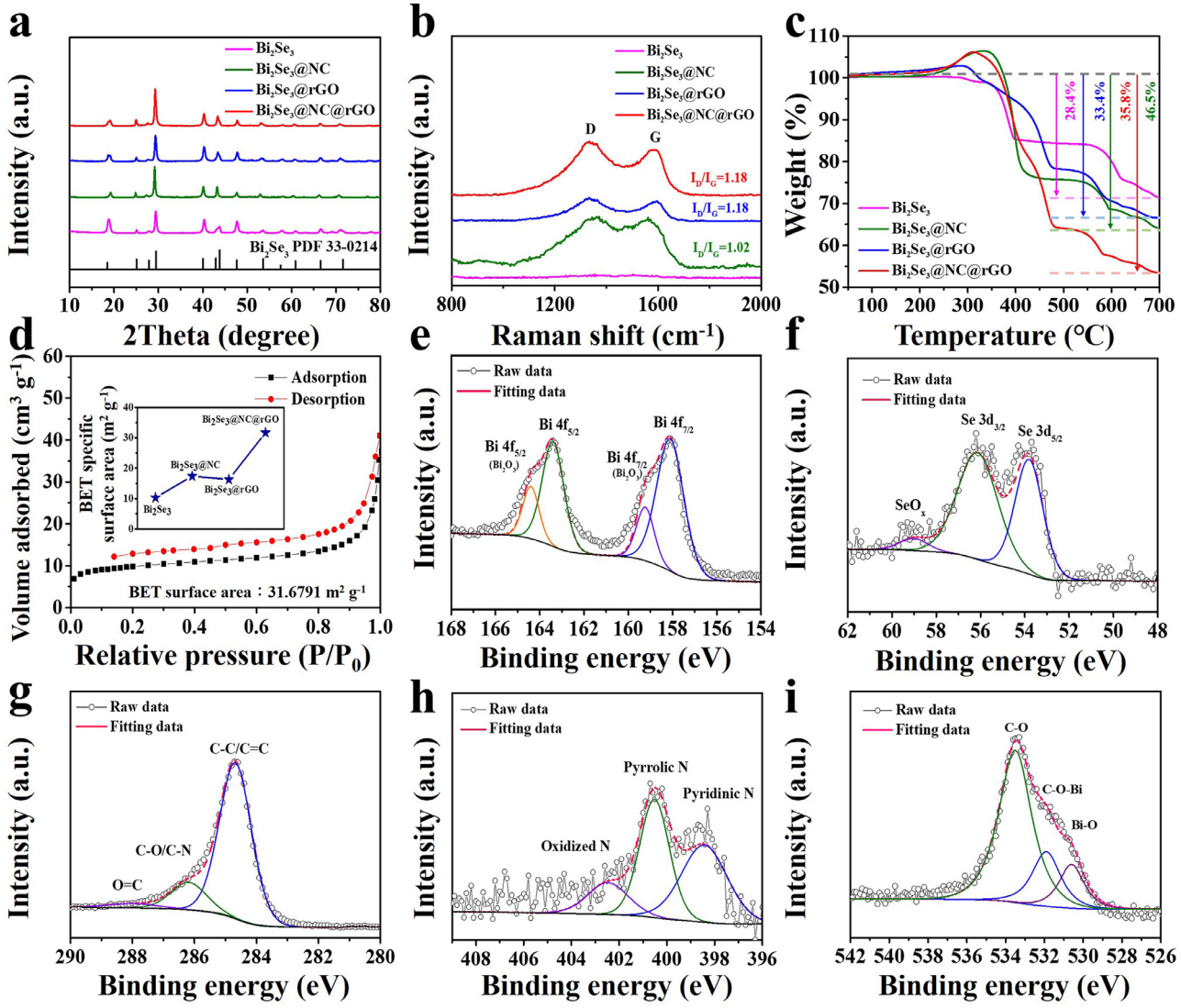

Fig. 2. Structure analysis: a) XRD patterns, b) Raman spectra, c) TGA profiles of Bi_2Se_3, Bi_2Se_3@NC, Bi_2Se_3@rGO and Bi_2Se_3@NC@rGO; d) nitrogen adsorption-desorption isotherm of Bi_2Se_3@NC@rGO, inset is the BET specific surface area for all samples; XPS, e) Bi 4f, f) Se 3d, g) C 1 s, h) N 1 s, and i) O 1 s fitting spectra of Bi_2Se_3@NC@rGO.

afore-stated approaches. The TEM and HRTEM images of the composite reveal distinct triple-layered architecture constructed by encapsulating Bi_2Se_3 nanosheets with a N-doped carbon-coating layer and flexible graphene outer shell (Fig. 1e–f). Moreover, field emission scanning electron microscopy (FESEM) and TEM images further indicate that both carbon coating and graphene confined the Bi_2Se_3 completely and uniformly in a large area in Fig. 1g–h and Fig. S5. The HRTEM image of Bi_2Se_3@NC@rGO in Fig. 1i shows that the clear lattice fringe with the interplanar spacing of 3.07 Å that is assigned to the (0 1 5) plane of the Bi_2Se_3 structure. The SAED pattern in Fig. 1j is ascribed to (1 0 4), (0 0 15), (1 2 5), (3 0 0) and (0 1 23) planes of the layered Bi_2Se_3 phase. The scanning TEM (STEM) and energy-dispersive X-ray spectrometry (EDS) mapping images displayed in Fig. 1k suggest successful construction of a triple-layered structure of Bi_2Se_3@NC@rGO with a homogenous distribution of Bi, Se, C, and N elements. The HRTEM images, SAED patterns, and EDS results also verify the structure and elemental composition of Bi_2Se_3, Bi_2Se_3@NC, and Bi_2Se_3@rGO as presented in Fig. S1h-i, Fig. S2d–f, and Fig. S3d–f , respectively.

Fig. 2a presents the XRD patterns of all samples, in which all diffraction peaks can be well indexed to the layered Bi_2Se_3 phase [34,35]. Raman spectra of Bi_2Se_3@NC, Bi_2Se_3@rGO, and Bi_2Se_3@NC@rGO in Fig. 2b display two peaks at 1345 and 1590 cm^{-1} attributed to the characteristic peaks of sp^3-hybridized disordered carbon (D-band) and sp^2-hybridized graphitic carbon (G-band), respectively [23,36,37]. Moreover, the high I_D/I_G values confirmed the existence of carbon-coating layer and graphene with amorphous nature [38, 39]. According to the thermogravimetric (TGA) result in Fig. 2c, the exact carbon and graphene content for Bi_2Se_3@NC, Bi_2Se_3@rGO, and Bi_2Se_3@NC@rGO could be calculated as 7.4%, 5.0%, and 18.1%, respectively. As shown in Fig. 2d and Fig. S6 , the N_2 adsorption/desorption isotherms exhibit typical type-IV curves with H4 hysteresis loops, thereby indicating a mesoporous structure, which is further demonstrated by the size distribution profiles (Fig. S7). The Bi_2Se_3@NC@rGO shows the highest Brunauer–Emmett–Teller (BET) specific surface area of 31.7 $m^2 \cdot g^{-1}$ than that of Bi_2Se_3 (10.3 $m^2 \cdot g^{-1}$), Bi_2Se_3@NC (17.4 $m^2 \cdot g^{-1}$), and Bi_2Se_3@rGO (16.3 $m^2 \cdot g^{-1}$) in the inset of Fig. 2d. This relatively high surface area can significantly contribute to efficient electrochemical kinetic behavior and provide a buffer area for mitigating volume expansion during the K-ion storage process.

The surface chemical composition and electronic structural information of the samples were investigated *via* X-ray photoelectron spectroscopy (XPS). In the high resolution of Bi 4f-fitting spectra (Fig. S8a,

Fig. S9a, Fig. S10a and Fig. 2e), two obvious peaks located at 163.4 and 158.1 eV correlated with Bi $4f_{5/2}$ and Bi $4f_{7/2}$ of Bi_2Se_3 [26,35]; this can also be observed for bare Bi_2Se_3, Bi_2Se_3@NC, Bi_2Se_3@rGO, and Bi_2Se_3@NC@rGO. Furthermore, the other two fitting peaks appear at 164.4 and 159.2 eV for all samples except Bi_2Se_3, which correspond to Bi $4f_{5/2}$ and Bi $4f_{7/2}$ of Bi_2O_3 [35], thereby showing that the surface of Bi_2Se_3 can be oxidized during the carbon coating and graphene wrapping process. There are couples of Se $3d_{3/2}$ and Se $3d_{5/2}$ peaks located at 56.2 and 53.9 eV (Fig. S8b, Fig. S9b, Fig. S10b, and Fig. 2f), signifying that the Se-ion is a negative bivalent [40], and the Se3d-fitting results further revealed the formation of SeO_x for all composites [41]. The appearance of both Bi_2O_3 and SeO_x demonstrates that the surface of the Bi_2Se_3 is tightly bound to the carbon-coating layer and graphene through an oxygen atom. Moreover, the C1s fitting spectra indicates three kinds of peaks attributed to C–C/C=C, C–O/C–N, and C=O [40,42], respectively, thereby suggesting the successful introduction of carbon coating and graphene (Fig. S9c, Fig. S10c, and Fig. 2g). As presented in Fig. S9d and Fig. 2h, the N 1 s spectra for Bi_2Se_3@NC and Bi_2Se_3@NC@rGO can be deconvoluted into three types of peaks at 402.5, 400.5, and 398.4 eV attributed to oxidized N, pyrrolic N, and pyridinic N [28,30,43]. Fig. 2i presents the O 1 s spectrum for Bi_2Se_3@NC@rGO, in which two fitting peaks with binding energies of 533.5 and 530.1 eV are assigned to C–O and Bi–O, respectively [35]. Furthermore, a strong split peak at 531.5 eV is assigned to the chemical bonding of C–O–Bi [35]; this contributes to fast charge transfer between Bi_2Se_3 and carbon and for excellent electrode stability in buffering the volume expansion upon cycling.

3.2. Electrochemical performances

The electrochemical properties of all electrodes were tested from 0.01 V to 3.0 V. The cyclic voltammetry (CV) was measured to clarify the redox behavior as shown in Fig. 3a. The two voltammetric reduction peaks of 0.86 V corresponding to the conversion reaction of Bi_2Se_3 and K to Bi and K_2Se can be observed for Bi_2Se_3@NC@rGO electrode during the first cathodic process. Also, there are distinct reduction peaks at 0.57 and 0.22 V, which could be attributed to the alloying process between Bi and K_3Bi [28,44]. In the initial anodic scan, the reversible dealloying peaks appear at 0.62, 0.87 and 1.23 V [28,44], whereas the oxidation peaks at 1.47, and 1.90 V are attributed to the reversed conversion process. Similar redox processes for K-ion storage can be obtained for the other three electrode materials, as presented in Fig. S11a, Fig. S12a, and Fig. S13a. Fig. 3b presents the charge/discharge curves of the initial five cycles at 100 $mA{\cdot}g^{-1}$ for Bi_2Se_3@NC@rGO composite. The curves display obvious slopes and plateaus, which is consistent with the redox behavior from the CV result. The CV and charge/discharge profiles overlapping upon the subsequent scanning, thereby suggesting superior electrochemical reversibility. Bi_2Se_3@NC@rGO delivers the highest first discharge/charge capacity of 931.5/612.0 $mAh{\cdot}g^{-1}$ compared to those of 757.0/508.9 $mAh{\cdot}g^{-1}$ for bare Bi_2Se_3 (Fig. S11b), 751.4/528.3 $mAh{\cdot}g^{-1}$ for Bi_2Se_3@NC (Fig. S12b), and 754.3/509.4 $mAh{\cdot}g^{-1}$ for Bi_2Se_3@rGO (Fig. S13b). The large initial irreversible capacity of Bi_2Se_3@NC@rGO is due to the formation of SEI film and the electrolyte decomposition.

As presented in Fig. 3c, Bi_2Se_3@NC@rGO displays the best cycling stability at 100 $mA{\cdot}g^{-1}$ than other electrodes, thereby maintaining a reversible capacity of 272.5 $mAh{\cdot}g^{-1}$ after 300 cycles higher than that of Bi_2Se_3 (1.4 $mAh{\cdot}g^{-1}$), Bi_2Se_3@NC (156.8 $mAh{\cdot}g^{-1}$), and Bi_2Se_3@rGO (104.2 $mAh{\cdot}g^{-1}$). The rate capability presented in Fig. 3d further highlights the advantage of the triple-layered architecture. The highest specific capacities of 504.7, 345.0, 281.1, 241.1, and 101.6 $mAh{\cdot}g^{-1}$ was achieved for Bi_2Se_3@NC@rGO at 200, 500, 1000, 2000, and 5000 $mA{\cdot}g^{-1}$, respectively. Fig. 3e displays the long-term cycling performance for the electrodes at 500 $mA{\cdot}g^{-1}$, and Bi_2Se_3@NC@rGO presents great cyclability with a capacity retention value of 113.5 $mAh{\cdot}g^{-1}$ over 1000 cycles, while the other three electrodes show severe capacity decay with retention values of 0.1, 46.1, and 22.9 $mAh{\cdot}g^{-1}$, respectively. The charge/discharge curves of the 50th,100th, 200th and 300th cycles at 100 $mA{\cdot}g^{-1}$ and the 200th, 400th, 600th, 800th and 1000th cycles at 500 $mA{\cdot}g^{-1}$ for Bi_2Se_3@NC@rGO are displayed in Fig. S14. It can be observed that the electrode exhibits highly reversible electrochemical process upon long cycles.

3.3. Electrochemical kinetics

Several techniques were used to investigate the electrochemical kinetics behavior of the electrodes. Excellent response capability can be achieved for the fast scan rate of Bi_2Se_3@NC@rGO from the CV profiles with analog shapes at different sweep rates (Fig. 4a); however, the other three electrodes exhibit poor response ability (Fig. S16, Fig. S17, and Fig. S18), most especially for the bare Bi_2Se_3. The equation $i = a\,v^b$ can describe the relationship between the measured current (i) and scanning rate (v), where the value of b can be determined from the slope of the linear fitting result of log (i) *vs.* log (v) [42,43]. The b values of 0.5 and 1 connote K-ion diffusion and surface capacitance contribution, respectively [45,46]. It can be seen from the fitting curves in Fig. 4b that the b values were calculated to be 0.803 and 0.745 during the oxidation process, thereby indicating that the capacity of Bi_2Se_3@NC@rGO is controlled by both diffusion and capacitive process. The exact quantitative result of both effects can be further determined *via* the equation $i = k_1 v + k_2 v^{1/2}$[23,47] Hence, the pseudocapacitive effect ($k_1 v$) and ions diffusion insertion process ($k_2 v^{1/2}$) can be calculated by ascertaining the constants of k_1 and k_2 based on the simplified equation of $i/v^{1/2} = k_1 v^{1/2} + k_2$. As displayed in Fig. 4c, the total capacity is dominant by the ion diffusion effect with the ratio of 56% at 0.1 $mV{\cdot}s^{-1}$. With an increase in the sweep rates, the percentage of capacitive-controlled behavior gradually rises and finally reached 70% at 1.0 $mV{\cdot}s^{-1}$; this shows that pseudo-capacitance plays an important role in K-ion storage at high scan rates, thus resulting in admirable rate property and cycling stability. The solid-state diffusion kinetics of K-ion for Bi_2Se_3@NC@rGO composite were investigated using galvanostatic intermittent titration technique (GITT) tested at 100 $mA{\cdot}g^{-1}$ (Fig. 4e). The K-ion diffusion coefficient ($D_K{}^+$) in Bi_2Se_3@NC@rGO electrode can be determined by according to the following Eq. (1): [48]

$$D_{k^+} = \frac{4}{\pi\tau}\left(\frac{m_B V_M}{M_B S}\right)^2\left(\frac{\Delta E_S}{\Delta E_\tau}\right)^2 \qquad \left(\tau \ll \frac{L^2}{D}\right) \tag{1}$$

where m_B is electrode active mass, M_B is the molar mass of the electrode material for Bi_2Se_3, V_M is the molar volume of Bi_2Se_3, τ is the current pulse time (s), S is the geometric area of the electrode, ΔE_S is the deviation of each equilibrium voltage, ΔE_τ is the deviation voltage during the current pulse (Fig. S19a), and L is the average thickness of electrode. Moreover, the calculated potassium ion diffusion coefficient ($D_K{}^+$) of Bi_2Se_3@NC@rGO remains almost the same order of magnitude (Fig. 4e), and the fluctuation is relatively stable compared with pure Bi_2Se_3 during charging (Fig. S19b), a high $D_K{}^+$ in the range of 10^{-8} to 10^{-9} $cm^2{\cdot}s^{-1}$ for discharge process and 10^{-9} to 10^{-10} $cm^2{\cdot}s^{-1}$ for charge process can be achieved, thereby demonstrating fast K-ion transport capability. In Electrochemical Impedance Spectrometry (EIS) spectra (Fig. S20), the values of charge-transfer resistance (R_{ct}) of Bi_2Se_3@NC@rGO are consistently lower than those of Bi_2Se_3 before cycling and after 10 cycles, indicating that the Bi_2Se_3@NC@rGO possesses a greater electrochemical kinetics behavior due to the inherent excellent characteristics of NC and rGO as well as the electron transfer contribution of C-O-Bi bond.

3.4. K-Ion storage mechanism

In situ XRD was employed to study the phase transformation behavior of Bi_2Se_3@rGO@NC and investigate the electrochemical mechanism during the K-ion insertion/extraction process (Fig. 5a–b). Upon the K-ion insertion into the Bi_2Se_3 host, then discharging to approximately

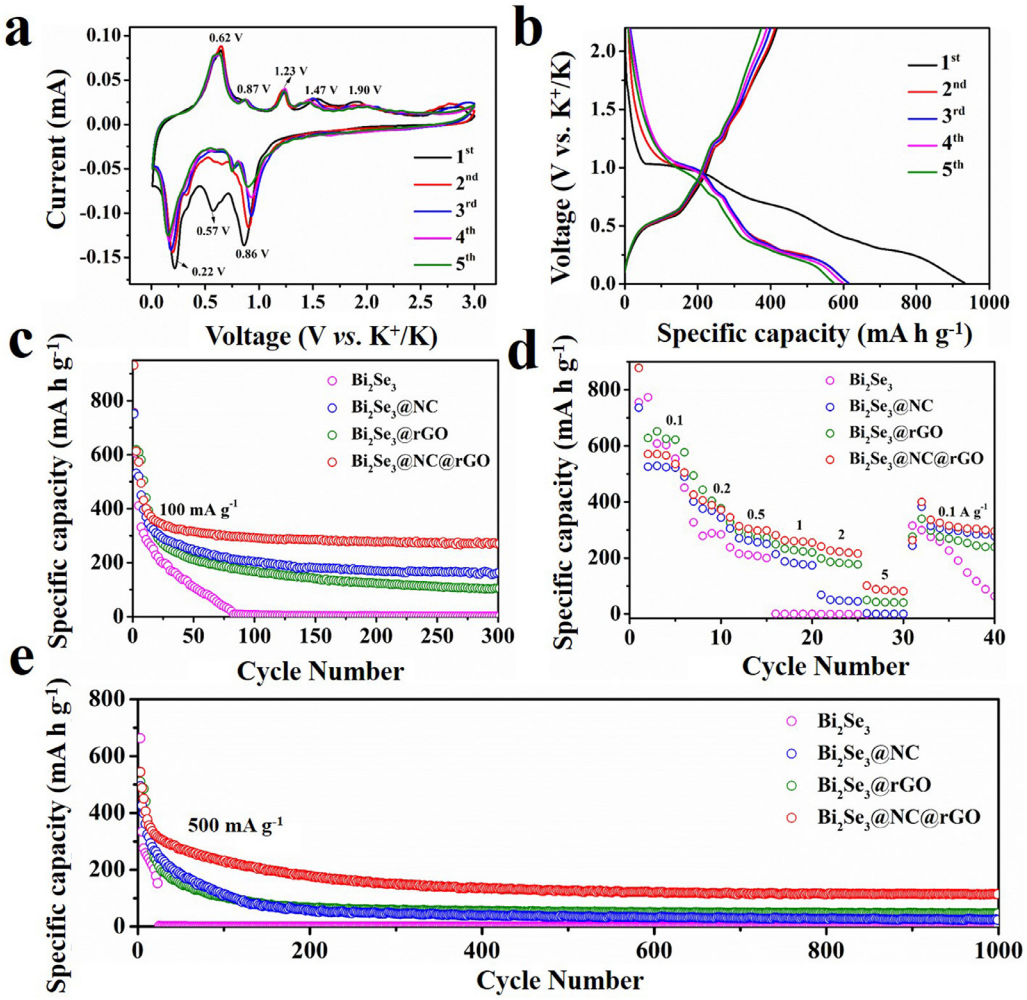

Fig. 3. K-ion storage performances: a) CV profiles of the initial five cycles at 0.1 $mV{\cdot}s^{-1}$ and b) galvanostatic charge/discharge curves at 100 $mA{\cdot}g^{-1}$ for Bi_2Se_3@NC@rGO; c) cyclic performance at 100 $mA{\cdot}g^{-1}$, d) rate property between 100 and 5000 $mA{\cdot}g^{-1}$ and e) long-term cycling curves at 500 $mA{\cdot}g^{-1}$ for the electrodes.

1.0 V (stage i → stage ii), the obvious diffraction peaks at 27.3°, 38.0°, and 39.8° were attributed to (0 1 2), (1 0 4), and (1 1 0) planes of Bi, while the peaks at 19.8° correspond to (1 1 1) facet of K_2Se, thus elucidating that the conversion reaction happens from Bi_2Se_3 and K to Bi and K_2Se. It is worth mentioning that the unique peaks at 25.4°, 28.5°, and 41.2° during the conversion process were assigned to (2 2 0), (3 1 0), and (0 2 4) facets of K_3BiSe_3, thereby suggesting that this conversion behavior was conducted in two successive steps with an intermediate product of K_3BiSe_3. After further discharging to approximately 0.6 V (stage ii → stage iii), the characteristic peaks of the KBi_2 phase occur at a position of 31.2° and 32.5° along with the disappearance of Bi structure, which reveals that Bi can be alloyed with K to form KBi_2. With the continuity of the K-ion insertion process between 0.01–0.6 V (stage iii → stage iv), KBi_2 gradually transform into K_3Bi, whose diffraction peaks at 18°, 29.4°, and 34.5° were assigned to (1 0 1), (1 0 3), and (2 0 1) planes [49,50]. Furthermore, K_3Bi stably exists at a fully discharged state, thus signifying that the alloying process reacts completely. During the initial charge process, the multistep dealloying reaction initially proceeds from K_3Bi to KBi_2 (stage iv → stage v). It then transforms into Bi (stage v → stage vi), and the reversible two-step conversion behavior with the reaction process of $Bi + 3\ K_2Se \rightarrow K_3BiSe_3 + 3\ K^+$ and $Bi + K_3BiSe_3 \rightarrow Bi_2Se_3 + 3\ K^+$ are presented in the reactions in stage (vi) to stage (vii). At the K-ion full extraction state (vii), the peaks located at 18.5°, 29.3°, 40.2°, and 42.9° were attributed to (0 0 6), (0 1 5), (1 0 10), and (0 1 11) facets of Bi_2Se_3 structure, thereby indicating high electrochemical reversibility. Except for the Bi_2Se_3 phase, K_3BiSe_3 and Bi do not completely disappear after charging at 3 V, thus indicating the absence of a thorough reversed conversion reaction. The *in situ* XRD line spots of the first, second and third cycles are shown in Fig. S21. It should be noted that during the second and third charge/discharge cycles, the K-ion storage process exhibits the same process as the first cycle, thus presenting a highly reversible potassiation/depotassiation behavior based on conversion-alloying dual mechanism. Hence, it can be found that the conversion product of K_2Se consistently exists during the alloying/dealloying reaction, thus signifying that K_2Se can act as a buffer zone to accommodate the volume expansion generated by the alloying process; this will also effectively release the stress, thereby maintaining great electrode integrity during cycling. Fig. 5c describes the specific electrochemical reaction process, where Bi_2Se_3@NC@rGO experiences reversible multistep conversion reaction of $Bi_2Se_3 + K^+ \leftrightarrow K_3BiSe_3 + Bi \leftrightarrow K_2Se + Bi$ and multistep alloying/dealloying process of $Bi + K^+ \leftrightarrow KBi_2 \leftrightarrow K_3Bi$. The *ex situ* TEM and FESEM images indicate that the morphology of the Bi_2Se_3@NC@rGO composite was efficiently preserved after 10 and 40 cycles (Fig. S22 and Fig. S23), thus signifying great structural stability of the triple-layered architecture upon the repeated K-ion insertion/extraction process.

An *ex situ* TEM analysis was conducted at different states of the first charge/discharge process to analyze the microstructure and investigate

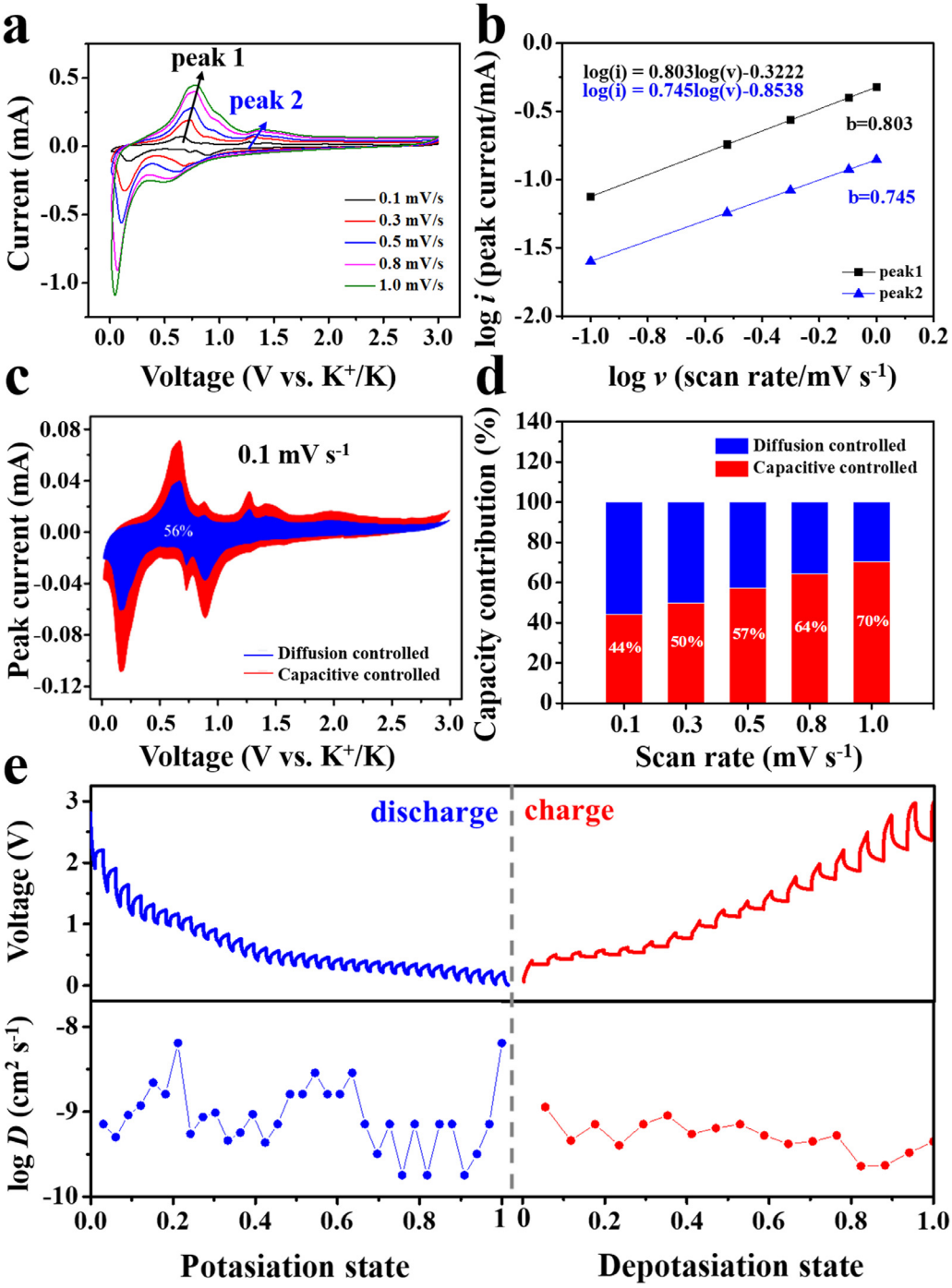

Fig. 4. Electrochemical kinetics behavior: a) CV curves at various sweep rates in the range of 0.1–1.0 mV·s^{-1}, b) linear fitting profiles of log I_p *vs.* log *v*, c) the CV profiles displaying the K-ions diffusion controlled contriution at 0.1 mV·s^{-1} and d) the percentage of diffusion and capacitive-controlled capacity contributions at different scanning rates of Bi_2Se_3@NC@rGO; e) GITT profiles of the first charge/discharge process at 100 mA·g^{-1} and the calculated K-ions diffusion coefficient for Bi_2Se_3@NC@rGO.

the detailed products of K-ion insertion/extraction for Bi_2Se_3@NC@rGO composite. The TEM image in the discharge state of 0.6 V (Fig. 6a) displays uniform nanosheet morphology tightly wrapped with graphene *via* a chemical bond of C–O–Bi, thereby presenting excellent structural stability for the triple-layered architecture. The corresponding SAED pattern (Fig. 6b) can be assigned to (4 2 2) and (3 3 1) facets of K_2Se phase and (4 2 2), (4 4 0), and (2 2 0) facets of KBi_2 phase, which agrees with the *in situ* XRD result. Furthermore, the presence of K_2Se further verifies that the conversion product plays an important part in buffering the large volume change during the alloying reaction. Fig. 6c presents an HRTEM image with a large area, thus showing noticeable lattice fringes with the distance of 2.75 Å, 2.37 Å, 1.76 Å, and 2.32 Å, which are assigned to (2 2 2) and (4 0 0) planes of KBi_2 as well as (3 3 1) and (3 1 1) planes of K_2Se, respectively. The EDS-mapping images demonstrate that K, Bi, Se, C, and N elements are homogeneously distributed throughout the triple-layered architecture (Fig. 6d). Even at the full K-ion insertion state, the robust 3D structure can still be maintained, as shown in Fig. 6e, thus highlighting the superiority of the composite. It can be ob-

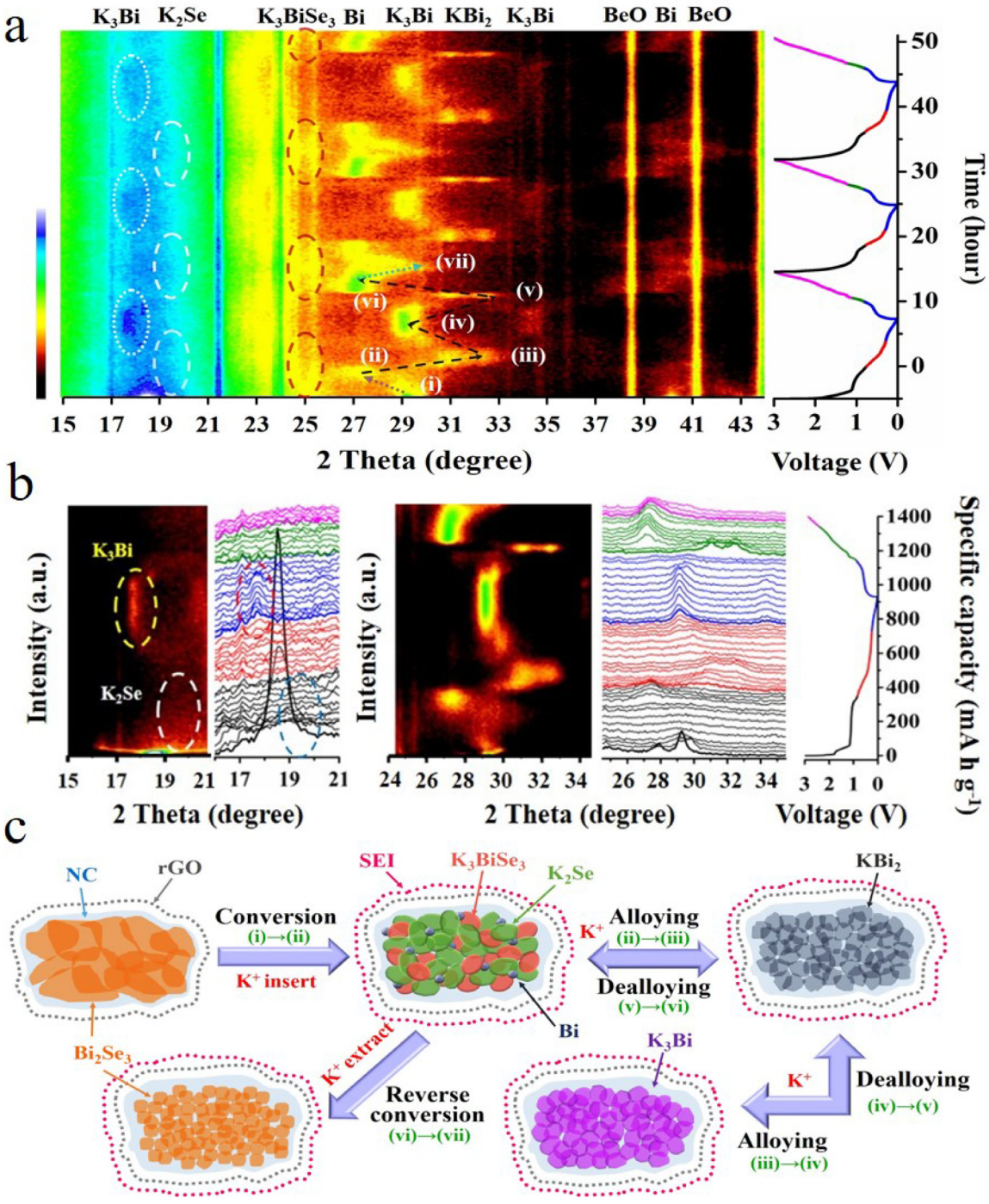

Fig. 5. Electrochemical reaction mechanism: a) *in situ* contour plot of the operando XRD result of Bi_2Se_3@NC@rGO electrode during the K-ion insetion/extraction process of the initial three cycles, b) *In situ* XRD patterns and corresponding line plots of Bi_2Se_3 electrode, and c) schematic view of the proposed electrochemical mechanism during the charge/discharge process.

served from the SAED pattern (Fig. 6f) and HRTEM image (Fig. 6g) that the final alloying product can be determined as K_3Bi. After charging to 3.0 V, the nanosheets were firmly confined into the graphene (Fig. 6h), thereby revealing that chemical bonding contributes to the electrode's outstanding stability. As displayed in Fig. 6i, the SAED pattern exhibits the (2 0 2) plane of Bi, (1 0 10) plane of Bi_2Se, and (3 1 0) plane of K_3BiSe_3; this is consistent with the HRTEM (Fig. 6j) and *in situ* XRD results. According to the *in situ* XRD and *ex situ* TEM analysis, the dual mechanisms of the conversion-alloying process were confirmed to affect the K-ion storage using a 12-electron transfer. The specific electrochemical process is summarized as follows:

Multistep conversion reaction:

$$Bi_2Se_3 + 3K^+ + 3e^- \leftrightarrow Bi + K_3BiSe_3 \quad (1a)$$

$$K_3BiSe_3 + 3K^+ + 3e^- \leftrightarrow Bi + 3K_2Se \quad (2)$$

Multistep alloying/dealloying reaction:

$$2Bi + K^+ + e^- \leftrightarrow KBi_2 \quad (3)$$

$$KBi_2 + 5K^+ + 5e^- \leftrightarrow 2K_3Bi \quad (4)$$

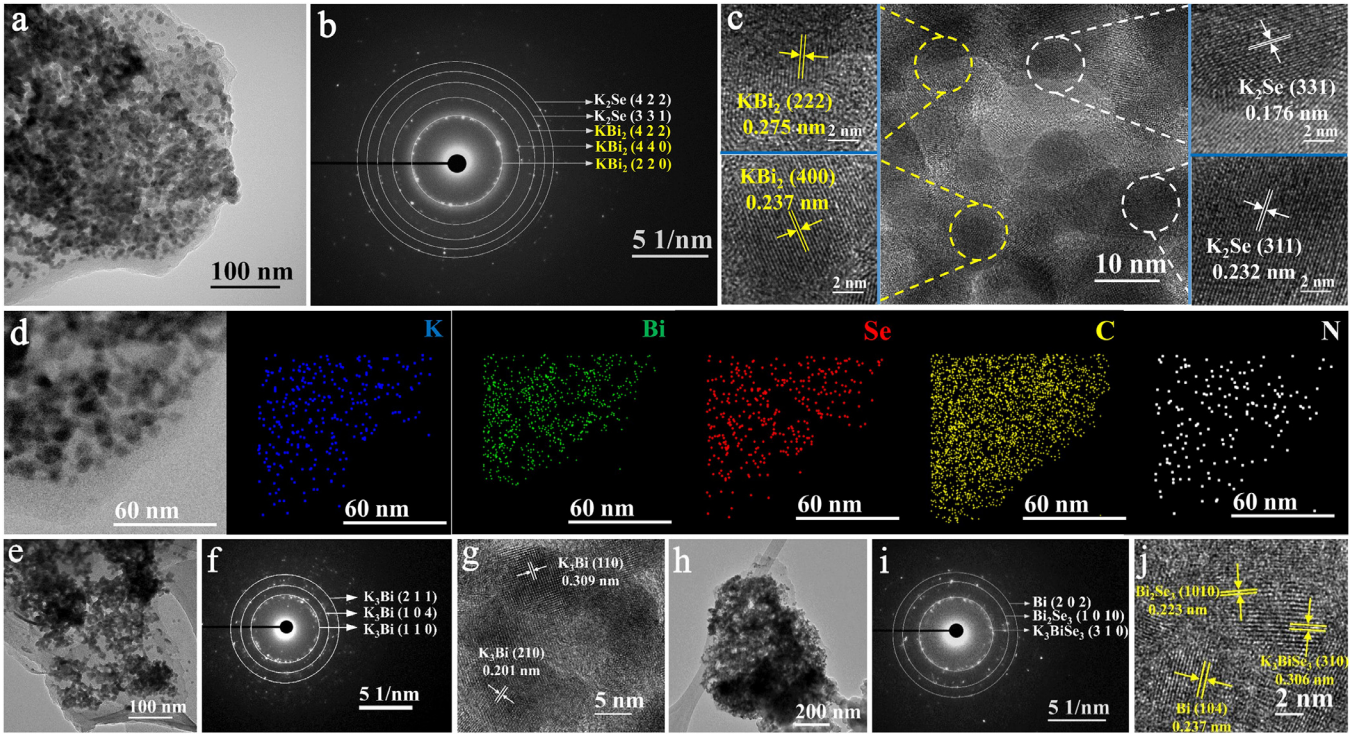

Fig. 6. Electrochemical reaction mechanism: a) TEM image, b) SAED pattern, c) HRTEM images, and d) EDS mapping images when discharging to 0.6 V during the first cycle; e) TEM image, f) SAED pattern and g) HRTEM image at the initial fully discharged state; h) TEM image, i) SAED pattern and j) HRTEM image at the initial fully charged state for Bi_2Se_3@NC@rGO.

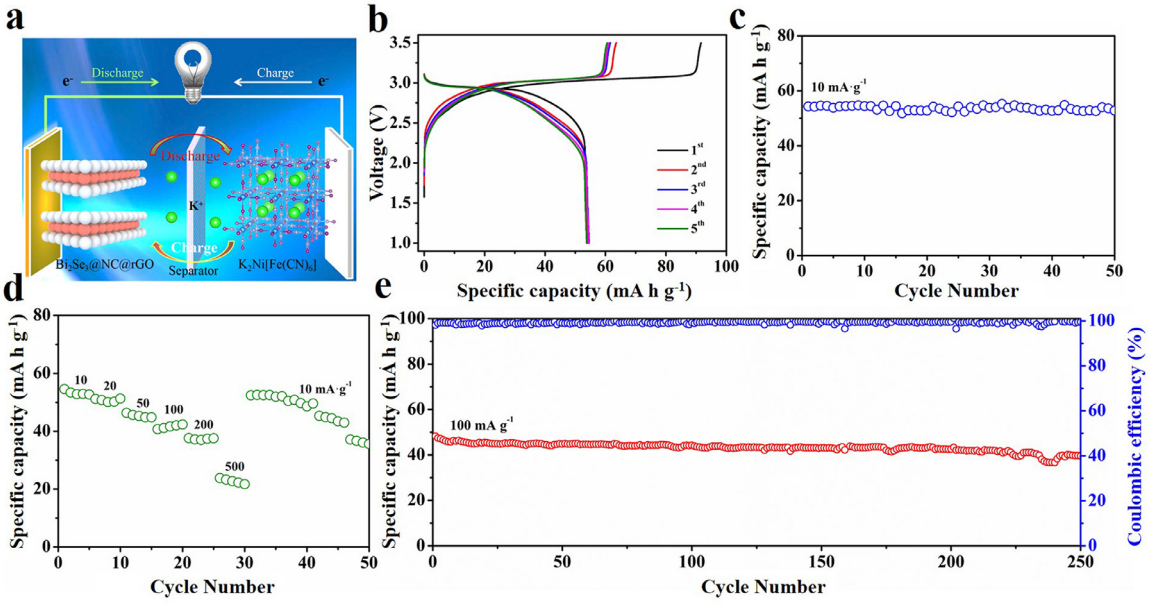

Fig. 7. The electrochemical performances of K-ion full cell using $K_2Ni[Fe(CN)_6]$ cathode and Bi_2Se_3@NC@rGO anode: a) assembly schematic of the full battery; b) galvanostatic charge/discharge profiles of the initial five cycles at 10 mA·g^{-1}, c) the cycling property at 10 mA·g^{-1}; d) the rate curve in the current densities range of 10 and 500 mA·g^{-1} and e) the cycling property at 100 mA·g^{-1}.

3.5. Full cell performances

The K-ion full batteries were assembled using $K_2Ni[Fe(CN)_6]$ cathode to confirm the actual availability of the triple-layered composite of Bi_2Se_3@NC@rGO, and the schematic drawing is revealed in Fig. 7a. The charge/discharge profiles of the first five cycles of the full cell exhibit clear redox plateaus (Fig. 7b), thus showing an initial reversible specific capacity of 54.3 mAh·g^{-1} with an operating voltage of 3.0 V and an energy density of 162.9 Wh·kg^{-1} at 10 mA·g^{-1}. Furthermore, a high specific capacity of 52.8 mAh·g^{-1} with a retention of 97.2% after 50 cycles were achieved (Fig. 7c), thus demonstrating exceptional cyclability. Fig. 7d presents the rate property and the specific capacities of 51.1, 46.3, 40.7, 37.6, and 23.8 mAh·g^{-1} at 20, 50, 100, 200, and 500 mA·g^{-1}, respectively. When the current density returns to 10

$mA{\cdot}g^{-1}$, a reversible capacity of 52.4 $mAh{\cdot}g^{-1}$ was recovered. Even at a high rate of 100 $mA{\cdot}g^{-1}$, the full battery delivers a high first capacity of 48.3 $mAh{\cdot}g^{-1}$ and admirable long-term cycling stability with a capacity retention of 39.5 $mAh{\cdot}g^{-1}$ over 250 cycles in Fig. 7e. Furthermore, the Coulombic efficiencies are close to 100% during cycling, thereby representing highly reversible K-ion intercalation/deintercalation behavior between the cathode and anode.

4. Conclusions

In summary, a comprehensive study on the Bi_2Se_3@NC@rGO composite as an anode based on the conversion-alloying dual mechanism was reported for PIBs. The resultant Bi_2Se_3@NC@rGO presents superior electrochemical performance, including a high first capacity of 612.0 $mAh{\cdot}g^{-1}$, admirable cyclability with a capacity retention of 272.5 $mAh{\cdot}g^{-1}$ over 300 cycles at 100 $mA{\cdot}g^{-1}$, good rate property with capacities of 241.1 $mAh{\cdot}g^{-1}$ (2 $A{\cdot}g^{-1}$) and 101.6 $mAh{\cdot}g^{-1}$ (5 $A{\cdot}g^{-1}$), and long lifespan with a retention of 113.5 $mAh{\cdot}g^{-1}$ over 1000 cycles at 500 $mA{\cdot}g^{-1}$. The outstanding K-ion storage properties can be attributed to the synergistic effect of the dual mechanism and the novel triple-layered composite with efficient K-ion diffusion and electron-transport capability, high-electrochemical reversibility, and extraordinary morphology stability, which is verified by the results of kinetics and *ex situ* techniques. In addition, the K-ion full battery using $K_2Ni[Fe(CN)_6]$ cathode was assembled to display a reversible capacity of 54.3 $mAh{\cdot}g^{-1}$ with an energy density of 162.9 $Wh{\cdot}kg^{-1}$. Therefore, this study not only scientifically clarifies the conversion-alloying dual mechanism but also brings guidance in studying a new-type anode for high-performance PIBs.

Declaration of Competing Interest

The authors declare that they have no known competing financial interests or personal relationships that could have appeared to influence the work reported in this paper.

CRediT authorship contribution statement

Kuan-Ting Chen: Conceptualization, Methodology, Data curtion. **Shaokun Chong:** Conceptualization, Writing – original draft. **Lingling Yuan:** Investigation. **Yi-Chun Yang:** Investigation. **Hsing-Yu Tuan:** Conceptualization, Resources, Supervision, Writing – review & editing.

Acknowledgements

This work was supported by the financial support from the Fundamental Research Funds for the Central Universities (G2020KY0534) and the Young Scholar Fellowship Program by Ministry of Science and Technology (Grant no. MOST 108-2636-E-007-013, and MOST 109-2636-E-007-011). H.-Y. Tuan also acknowledges the financial support of National Tsing Hua University through the grant of 109QI030E1.

Supplementary materials

Supplementary material associated with this article can be found, in the online version, at doi:10.1016/j.ensm.2021.04.019.

References

[1] J.W. Choi, D. Aurbach, Promise and reality of post-lithium-ion batteries with high energy densities, Nat. Rev. Mater. 1 (2016) 16013.
[2] M. Li, J. Lu, Z. Chen, K. Amine, 30 years of lithium-ion batteries, Adv. Mater. 30 (2018) 1800561.
[3] S. Chen, C. Wu, L. Shen, C. Zhu, Y. Huang, K. Xi, J. Maier, Y. Yu, Challenges and perspectives for NASICON-type electrode materials for advanced sodium-ion batteries, Adv. Mater. 29 (2017) 1700431.
[4] Y.S. Xu, S.Y. Duan, Y.G. Sun, D. Bin, X.S. Tao, D. Zhang, Y. Liu, A.M. Cao, L.J. Wan, Recent developments in electrode materials for potassium-ion batteries, J. Mater. Chem. A. 7 (2019) 4334–4352.
[5] H. Wang, D. Yu, X. Wang, Z. Niu, M. Chen, L. Cheng, W. Zhou, L. Guo, Electrolyte chemistry enables simultaneous stabilization of potassium metal and alloying anode for potassium-ion batteries, Angew. Chem. Int. Ed. 58 (2019) 6451–16455.
[6] S. Chong, J. Yang, L. Sun, S. Guo, Y. Liu, H.K. Liu, Potassium nickel iron hexacyanoferrate as ultra-long-life cathode material for potassium-ion batteries with high energy density, ACS Nano 14 (2020) 9807–9818.
[7] W. Zhang, Y. Liu, Z. Guo, Approaching high-performance potassium-ion batteries via advanced design strategies and engineering, Sci. Adv. 5 (2019) 7412.
[8] S.-B. Huang, Y.-Y. Hsieh, K.-T. Chen, H.-Y. Tuan, Flexible nanostructured potassium-ion batteries, Chem. Eng. J. (2020) 127697.
[9] W. Zhang, W.K. Pang, V. Sencadas, Z. Guo, Understanding high-energy-density Sn_4P_3 anodes for potassium-ion batteries, Joule 2 (2018) 1534–1547.
[10] Q. Zhang, J. Mao, W.K. Pang, T. Zheng, V. Sencadas, Y. Chen, Y. Liu, Z. Guo, Boosting the potassium storage performance of alloy-based anode materials via electrolyte salt chemistry, Adv. Energy Mater. 8 (2018) 1703288.
[11] Q. Zhang, J. Mao, W.K. Pang, T. Zheng, V. Sencadas, Y. Chen, Y. Liu, Z. Guo, Boosting the potassium storage performance of alloy-based anode materials via electrolyte salt chemistry, Adv. Energy Mater. 8 (2018) 1703288.
[12] S. Chong, Y. Wu, C. Liu, Y. Chen, G. Cao, Y. Liu, G. Gao, Cryptomelane-type MnO_2/carbon nanotube hybrids as bifunctional electrode material for high capacity potassium-ion full batteries, Nano Energy 54 (2018) 106.
[13] X. Wu, D.P. Leonard, X. Ji, Emerging non-aqueous potassium-ion batteries: challenges and opportunities, Chem. Mater. 29 (2017) 5031–5042.
[14] J. Zhang, T. Liu, X. Cheng, M. Xia, R. Zheng, N. Peng, H. Yu, M. Shui, J. Shu, Development status and future prospect of non-aqueous potassium ion batteries for large scale energy storage, Nano Energy 60 (2019) 340–361.
[15] Q. Zhang, Z. Wang, S. Zhang, T. Zhou, J. Mao, Z. Guo, Cathode materials for potassium-ion batteries: current status and perspective, Electrochem. Energy Rev. 1 (2018) 625–658.
[16] H. Kim, H. Ji, J. Wang, G. Ceder, Next-generation cathode materials for non-aqueous potassium-ion batteries, Trends Chem. 1 (2019) 682–692.
[17] Y.H. Zhu, X. Yang, D. Bao, X.F. Bie, T. Sun, S. Wang, Y.S. Jiang, X.B. Zhang, J.M. Yan, Q. Jiang, High-energy-density flexible potassium-ion battery based on patterned electrodes, Joule 2 (2018) 736–746.
[18] R. Berthelot, V. Gabaudan, L. Monconduit, L. Stievano, Snapshot on negative electrode materials for potassium-ion batteries, Front. Energy Res. 7 (2019) 46.
[19] H. Tan, Y. Feng, X. Rui, Y. Yu, S. Huang, Metal chalcogenides: paving the way for high-performance sodium/potassium-ion batteries, Small Methods 4 (2020) 1900563.
[20] X. Wu, Y. Chen, Z. Xing, C.W.K. Lam, S.-S. Pang, W. Zhang, Z. Ju, Advanced carbon-based anodes for potassium-ion batteries, Adv. Energy Mater. 9 (2019) 1900343.
[21] L. Fan, R. Ma, Q. Zhang, X. Jia, B. Lu, Graphite anode for a potassium-ion battery with unprecedented performance, Angew. Chem., Int. Ed. 58 (2019) 10500–10505.
[22] W. Yang, J. Zhou, S. Wang, W. Zhang, Z. Wang, F. Lv, K. Wang, Q. Sun, S. Guo, Freestanding film made by necklace-like N-doped hollow carbon with hierarchical pores for high-performance potassium-ion storage, Energy Environ. Sci. 12 (2019) 1605–1612.
[23] S. Chong, L. Sun, C. Shu, S. Guo, Y. Liu, W.A. Wang, H.K. Liu, Chemical bonding boosts nano-rose-like MoS_2 anchored on reduced graphene oxide for superior potassium-ion storage, Nano Energy 63 (2019) 103868.
[24] C. Yang, J. Feng, F. Lv, J. Zhou, C. Lin, K. Wang, Y. Zhang, Y. Yang, W. Wang, J. Li, S. Guo, Metallic graphene-like VSe_2 ultrathin nanosheets: superior potassium-ion storage and their working mechanism, Adv. Mater. 30 (2018) 1800036.
[25] S. Chen, F. Wu, L. Shen, Y. Huang, S.K. Sinha, V. Srot, P.A. van Aken, J. Maier, Y. Yu, Cross-linking hollow carbon sheet encapsulated CuP_2 nanocomposites for high energy density sodium-ion batteries, ACS Nano 12 (2018) 7018–7027.
[26] K.-T. Chen, H.-Y. Tuan, Bi–Sb nanocrystals embedded in phosphorus as high-performance potassium ion battery electrodes, ACS Nano 14 (2020) 11648–11661.
[27] W.-C. Chang, J.-H. Wu, K.-T. Chen, H.-Y. Tuan, Red phosphorus potassium-ion battery anodes, Adv. Sci. 6 (2019) 1801354.
[28] H. Yang, R. Xu, Y. Yao, S. Ye, X. Zhou, Y. Yu, Multicore–Shell Bi@N-doped carbon nanospheres for high power density and long cycle life sodium- and potassium-ion anodes, Adv. Funct. Mater. 29 (2019) 1809195.
[29] Y. Liu, Z. Tai, J. Zhang, W.K. Pang, Q. Zhang, H. Feng, K. Konstantinov, Z. Guo, H.K. Liu, Boosting potassium-ion batteries by few-layered composite anodes prepared via solution-triggered one-step shear exfoliation, Nat. Commun. 9 (2018) 3645.
[30] S. Wang, P. Xiong, X. Guo, J. Zhang, X. Gao, F. Zhang, X. Tang, P.H.L. Notten, G. Wang, A stable conversion and alloying anode for potassium-ion batteries: a combined strategy of encapsulation and confinement, Adv. Funct. Mater. 30 (2020) 2001588.
[31] L. Fang, J. Xu, S. Sun, B. Lin, Q. Guo, D. Luo, H. Xia, Few-layered tin sulfide nanosheets supported on reduced graphene oxide as a high-performance anode for potassium-ion batteries, Small 15 (2019) 1804806.
[32] D.S. Bin, S.Y. Duan, X.J. Lin, L. Liu, Y. Liu, Y.S. Xu, Y.G. Sun, X.S. Tao, A.M. Cao, L.J. Wan, Structural engineering of SnS_2/graphene nanocomposite for high-performance K-ion battery anode, Nano Energy 60 (2019) 912–918.
[33] S. Chong, Y. Wu, S. Guo, Y. Liu, G. Cao, Potassium nickel hexacyanoferrate as cathode for high voltage and ultralong life potassium-ion batteries, Energy Storage Mater. 22 (2020) 120–127.
[34] P. Kumari, R. Singh, K. Awasthi, T. Ichikawa, A. Jain, Highly stable nanostructured Bi_2Se_3 anode material for all solid-state lithium-ion batteries, J. Alloys Compounds 838 (2020) 155403.
[35] D. Li, J. Zhou, X. Chen, H. Song, Graphene-loaded Bi_2Se_3: a conversion–alloying-type anode material for ultrafast gravimetric and volumetric Na storage, ACS Appl. Mater. Interfaces 10 (2018) 30379.

[36] Z. Tong, R. Yang, S. Wu, D. Shen, T. Jiao, K. Zhang, W. Zhang, C.S. Lee, Surface-engineered black niobium oxide@graphene nanosheets for high-performance sodium-/potassium-ion full batteries, Small 15 (2019) 1901272.
[37] H. Huang, J. Cui, G. Liu, R. Bi, L. Zhang, Carbon coated $MoSe_2$/MXene hybrid nanosheets for superior potassium storage, ACS Nano 13 (2019) 3448–3456.
[38] P. Lu, Y. Sun, H.F. Xiang, X. Liang, Y. Yu, 3D amorphous carbon with controlled porous and disordered structures as a high-rate anode material for sodium-ion batteries, Adv. Energy Mater. 8 (2018) 1702434.
[39] Z. Wu, G. Liang, W.K. Pang, T. Zhou, Z. Cheng, W. Zhang, Y. Liu, B. Johannessen, Z. Guo, Coupling topological insulator $SnSb_2Te_4$ nanodots with highly doped graphene for high-rate energy storage, Adv. Mater. 32 (2020) 1905632.
[40] Z. Yi, Y. Qian, J. Tian, K. Shen, N. Lin, Y. Qian, Self-templating growth of Sb_2Se_3@C microtube: a convention-alloying-type anode material for enhanced K-ion batteries, J. Mater. Chem. A 7 (2019) 12283–12291.
[41] R. Xu, T. Yao, H. Wang, Y. Yuan, J. Wang, H. Yang, Y. Jiang, P. Shi, X. Wu, Z. Peng, Z.-S. Wu, J. Lu, Y. Yu, Unraveling the nature of excellent potassium storage in small-molecule Se@peapod-like N-doped carbon nanofibers, Adv. Mater. 32 (2020) 2003879.
[42] Z. Yi, Y. Qian, S. Jiang, Y. Li, N. Lin, Y. Qian, Self-wrinkled graphene as a mechanical buffer: a rational design to boost the K-ion storage performance of Sb_2Se_3 nanoparticles, Chem. Eng. J. 379 (2020) 122352.
[43] W. Luo, F. Li, W. Zhang, K. Han, J.J. Gaumet, H.E. Schaefer, L. Mai, Encapsulating segment-like antimony nanorod in hollow carbon tube as long-lifespan, high-rate anodes for rechargeable K-ion batteries, Nano Res. 12 (2019) 1025–1031.
[44] S. Qi, X. Xie, X. Peng, H.L.N. Dickon, M. Wu, Q. Liu, J. Yang, J. Ma, Mesoporous carbon-coated bismuth nanorods as anode for potassium-ion batteries, Phys. Status Solidi RRL 13 (2019) 1900209.
[45] J. Xie, Y. Zhu, N. Zhuang, H. Lei, W. Zhu, Y. Fu, M.S. Javed, J. Li, W. Mai, Rational design of metal organic framework-derived FeS_2 hollow Nanocages@Reduced graphene oxide for K-ion storage, Nanoscale 10 (2018) 17092–17098.
[46] Z. Liu, P. Li, G. Suo, S. Gong, W.A. Wang, C.-Y. Lao, Y. Xie, H. Guo, Q. Yu, W. Zhao, K. Han, Q. Wang, M. Qin, K. Xi, X. Qu, Zero-strain $K_{0.6}Mn_1F_{2.7}$ hollow nanocubes for ultrastable potassium ion storage, Energy Environ. Sci. 11 (2018) 3033–3042.
[47] H. Wu, Q. Yu, C.Y. Lao, M. Qin, W. Wang, Z. Liu, C. Man, L. Wang, B. Jia, X. Qu, Scalable synthesis of VN quantum dots encapsulated in ultralarge pillared N-Doped mesoporous carbon microsheets for superior potassium storage, Energy Storage Mater. 18 (2018) 43–50.
[48] S. Dong, D. Yu, J. Yang, L. Jiang, J. Wang, L. Cheng, Y. Zhou, H. Yue, H. Wang, L. Guo, Tellurium: a high-volumetric-capacity potassium-ion battery electrode material, Adv. Mater. 32 (2020) 1908027.
[49] J. Huang, X. Lin, H. Tan, B. Zhang, Bismuth microparticles as advanced anodes for potassium-ion battery, Adv. Energy Mater. 8 (2018) 1703496.
[50] Y. Zhao, X. Ren, Z. Xing, D. Zhu, W. Tian, C. Guan, Y. Yang, W. Qin, J. Wang, L. Zhang, Y. Huang, W. Wen, X. Li, R. Tai, In situ formation of hierarchical bismuth nanodots/graphene nanoarchitectures for ultrahigh-rate and durable potassium-ion storage, Small 16 (2020) 1905789.